Composites Part A 131 (2020) 105783

Contents lists available at ScienceDirect

Composites Part A

journal homepage: www.elsevier.com/locate/compositesa

An experimental study on the influence of intralaminar damage on interlaminar delamination properties of laminated composites

Ping Hu, Ditho Pulungan, Ran Tao, Gilles Lubineau*

King Abdullah University of Science and Technology (KAUST), Physical Science and Engineering Division, COHMAS Laboratory, Thuwal 23955-6900, Saudi Arabia

ARTICLE INFO

Keywords:
Coupling
Transverse cracks
Delamination
Fiber bridging

ABSTRACT

Coupling between intralaminar and interlaminar damage plays a significant role in accurately predicting delamination and final failure. However, insufficient experimental data are available for models of this phenomenon. In this paper, we proposed a two-step experiment on cross-ply laminates to quantitatively study the influence of in-plane strain on the interlaminar fracture toughness. First, we performed a tensile test on the $[0_2/90_2]_s$ cross-ply laminates to introduce various extents of intralaminar damage. Next, we bonded a backing adherend of $[0_6]$ plies to the cross-ply, so we could probe the delamination properties through a subsequent double cantilever beam (DCB) test. We identified the effective fracture toughness $G_{c,\mathrm{eff}}$ by the compliance calibration method. We found that intralaminar damage promotes fiber bridging in the transverse direction, which finally influence the out-of-plane properties significantly.

1. Introduction

Recent decades have seen the rapid deployment of light and high strength materials in the aerospace industries. Carbon fiber-reinforced polymer (CFRP) composites have strong in-plane strength and excellent corrosion resistance compared to aluminum alloy. Thus, their damage mechanisms and the relevant modeling approaches have been extensively studied [1–3]. The failure process of laminated composites is complex, including diffuse matrix damage, transverse cracks, local delamination, fiber breakage and/or buckling/delamination [4–6]. Depending on the exact material properties, stacking sequence and boundary conditions, the dominant failure mechanisms can vary significantly resulting from the combination of the elementary mechanisms cited above.

One of the most critical degradation modes of laminated composites is delamination. Due to the relatively low strength of the matrix, laminated composites are quite weak under out-of-plane loading. A tool drop during maintenance could cause delamination at the interface between layers with different orientations [7], and result in barely visible impact damage (BVID). BVID does not significantly affect the tensile strength; however, it could significantly decrease the residual strength under compressive loading, leading to a catastrophic failure [8]. For this reason, predictive delamination models have raised massive interest from both industry and academic fields.

For any macroscopic propagation of cracks, delamination is composed of two main stages: the initiation stage, followed by the propagation stage. Initiation is usually triggered by stress concentrations arising from geometrical singularities (edges, holes, etc.) or intralaminar artifacts such as transverse cracks. Many studies showed this essential role of transverse cracking onto delamination by performing tensile loading or impact tests [9,10]. For example, using CT images of the delaminated area in a quasi-static indentation (QSI) test, Abisset et al. [11] clearly demonstrated that transverse cracks in adjacent plies correlate with delamination area. Patrick et al. [12] performed a uniaxial tension test on different ply orientations to study damage initiation and propagation. The resulting X-ray images indicated that the delamination initiated from the surrounding transverse cracks.

During the propagation stage, delamination toughness is characterized by the joint contribution of local (deriving the point-to-point failure of the adhesive of the interface of the joint) and non-local dissipation such as fiber bridging. Such a non-local contribution generally increases resistance towards delamination, as shown in the R-curve [13,14]. Moura et al. evaluated the bridging effect by cutting the bridging fibers during crack propagation in interlaminar and intralaminar mode I fracture test [15]. They found that fiber bridging accounts for 60% of the measured energy dissipated during interlaminar delamination propagation. They also showed that due to more fiber bridging, the intralaminar fracture toughness is higher than the interlaminar one. After cutting the bridging fibers, the fracture toughness for interlaminar and intralaminar are quite similar. This suggested

* Corresponding author.
E-mail address: gilles.lubineau@kaust.edu.sa (G. Lubineau).

https://doi.org/10.1016/j.compositesa.2020.105783
Received 22 October 2019; Received in revised form 6 January 2020; Accepted 19 January 2020
Available online 24 January 2020
1359-835X/

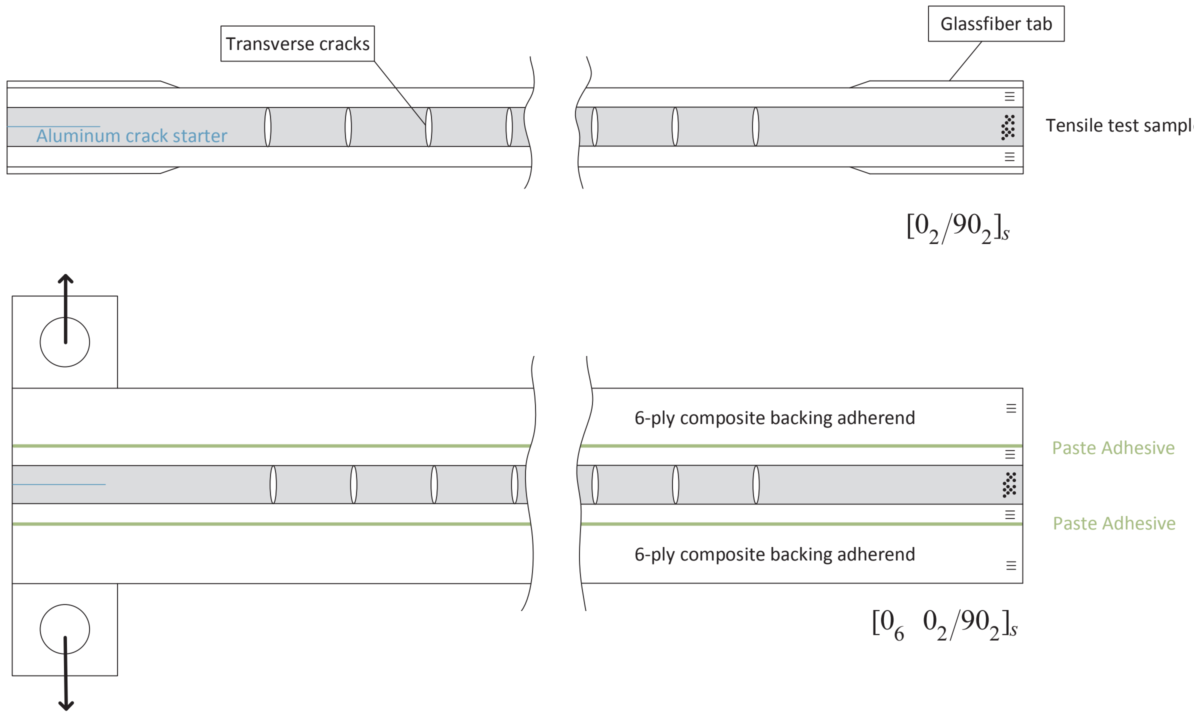

Fig. 1. Experimental plan of DCB after tensile test. (For interpretation of the references to colour in this figure legend, the reader is referred to the web version of this article.)

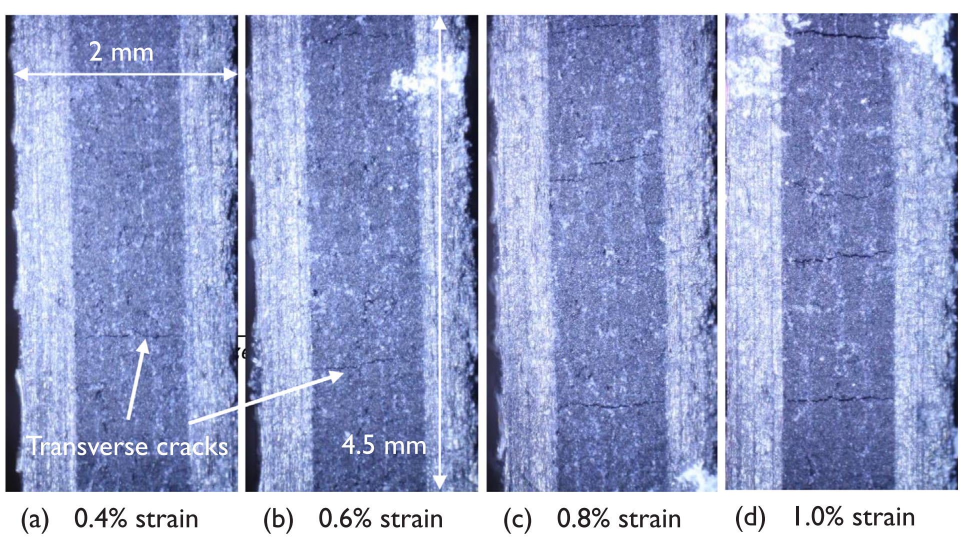

Fig. 2. Examples of different transverse crack densities. (For interpretation of the references to colour in this figure legend, the reader is referred to the web version of this article.)

that, while the toughness related to the local part of the dissipation is a material property, the dissipation due to bridging is a structural effect. Farmand-Ashtiani et al. [16] conducted DCB tests with different adherent thicknesses. They showed that the variation of the beam's curvature in the bridging zone due to different thickness changed the rate of traction decay, leading to a different steady energy release rate (ERR).

In all cases mentioned above, the analyses were performed on pristine laminates. During the the lifetime of a structure, the laminate could be pre-damaged due to in-plane loading. To the authors' knowledge, only a few studies have been done on how the intralaminar damage influences the subsequent delamination resistance. Huchette et al. [17] designed a two-step test in which they first performed a tensile test on $[0_2/90_2]_s$ to create transverse cracks in 90° plies. Then, they introduced a notch at the middle of 0° plies to trigger delamination when the laminate was pulled apart. They found that by introducing more intralaminar damage, the propagation of the delamination between the 0/90 interface occurs earlier. However, the load measured from such tests was dominated by the 0° plies rigidity, and large scatters of experimental results were observed. Therefore, they cannot characterize the change in delamination toughness due to the intralaminar damage.

In this paper, we designed a two-step experiment on cross-ply laminates to quantitatively characterize the coupling effect between the intralaminar damage and interlaminar property. First, cross-ply $[0_2/90_2]_s$ laminates were pulled at different strain levels to create various extents of intralaminar damage (transverse cracking density). Next, a backing adherend of $[0_6]$ plies was bonded to each side of $[0_2/90_2]_s$.

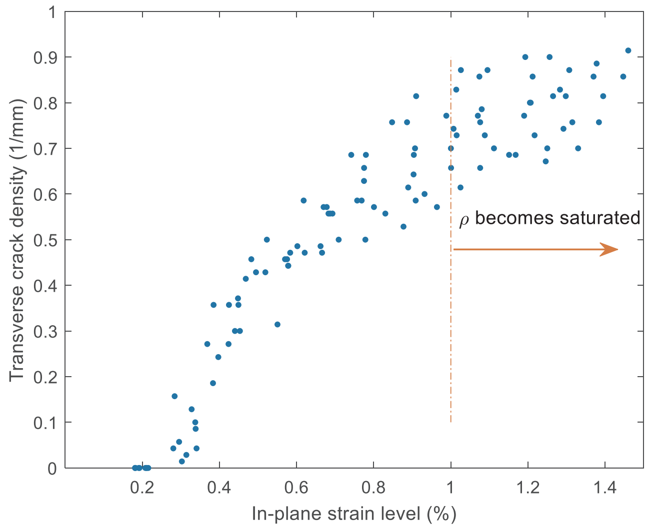

Fig. 3. Transverse crack density evolution with respect to in-plane strain. (For interpretation of the references to colour in this figure legend, the reader is referred to the web version of this article.)

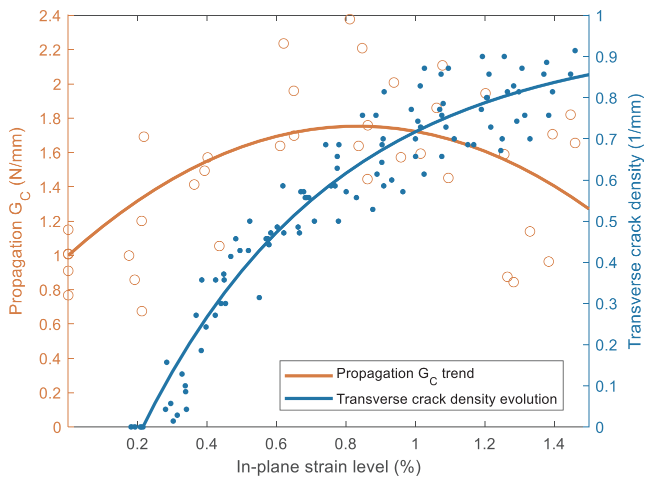

Fig. 4. Comparison of the propagation G_c evolution and transverse crack density evolution. (For interpretation of the references to colour in this figure legend, the reader is referred to the web version of this article.)

Then, we performed double cantilever beam (DCB) tests on these back bonded $[0_6||0_2/90_2]_s$ samples, where '||' denotes the back bonding position. The effective fracture toughness $G_{c,\mathrm{eff}}$ was finally calculated based on ASTM standard D5528 [18]. This original experimental strategy provides direct information about the influence of the in-plane loading on the out-of-plane properties; thus, modeling parameters can be identified accurately.

Following this introduction, Section 2 describes the experimental procedures and materials in detail. Section 3 presents the experimental results of the DCB test on pre-damaged samples. We evaluated the influence of various in-plane tensile strain level on the effective fracture toughness. We performed endoscopy and CT-scan analysis to study the fiber bridging morphology. We also conducted tests with a different width to support our findings. Section 4 concludes this paper with some general remarks about our results can be the starting point for future works aiming at enhancing classical modeling approaches.

2. Experiments

2.1. Proposed experimental procedures

We designed a two-step experiment on cross-ply laminates to quantitatively characterize the change in interlaminar property due to various intralaminar damage levels (see Fig. 1). In the first step, the cross-ply $[0_2/90_2]_s$ samples were pulled up to specific in-plane strain levels (from 0% to 1.4% with 0.2% interval) to introduce a wide range of transverse crack densities. The maximum strain of 1.4% was chosen right below the expected fiber breakage. For each strain level, we tested five samples to ensure statistically representative data. An Instron 5882 test frame (100 kN load cell) was used and strains were measured using a built-in Instron video extensometer. The loading speed was set at 1 mm/min to reach a constant strain rate level of 10^{-4}/s, a low enough rate to be considered as quasi-static loading. We stopped the tensile frame when the targeted strain level was reached. Note that a small deviation might exist between the targeted strain and the stopping strain due to the loading system. Yet, the real applied macroscopic strain was always used as a reference and is the value reported in all tests.

While observation of transverse cracking is convenient in glass fiber-based laminates due to its transparency [19], counting transverse cracks in carbon fiber-based laminates requires special care. It is not transparent, and therefore, X-ray with zinc iodide are usually used to count the transverse cracks [20] and to clearly identify whether these are fully percolated throughout the full width of the samples. Yet, interrupting the test and using zinc iodide may influence the response of the laminate [21,22]. In this work, we manually counted the number of transverse cracks by imaging the free edge of the sample. These images were taken by a DSLR camera attached to a Questar QM100 long-distance microscope. We assumed that the number of transverse cracks appearing at the edges is equivalent to the number of fully percolated cracks, as shown in [23]. This is also supported by the work of Nairn et al. [24], where for $n \geqslant \frac{m}{2}$ in the $[0_m/90_n]_s$ laminates, the edge crack will instantaneously extend to the full width of the sample. This condition was fulfilled in our stacking sequence (m = 2, n = 2).

The pre-damaged samples were subsequently subjected to a DCB test following the ASTM standard D5528 [18]. To follow the thickness (3 to 5 mm) recommended by the ASTM standard, we back-bonded a $[0_6]$ unidirectional ply to each side of the pre-damaged sample to provide extra bending stiffness [25–27], resulting in a $[0_6||0_2/90_2]_s$ sample. Such a back-bonding strategy enabled us to perform a tensile test with a thin 0° ply and hence, the 1.4% tensile strain level could be achieved by the available load cell (100 kN) in our research facility.

Uniform pressure was applied across the samples, utilizing clamps to ensure proper back-bonding. Then, they were put inside an oven at 60°C for at least four hours to accelerate the curing process. Aluminum blocks were then glued to the DCB samples and the DCB tests were carried out with an Instron 5882 test frame (500 N load cell) at a speed of 2 mm/min following the ASTM standard D5528 [18]. The compliance calibration (CC) method was used to calculate the effective toughness $G_{c,\mathrm{eff}}$ (see [18] for more details). Note that the DCB test may result in an unsymmetrical DCB crack propagation since delamination migration may occur and the crack may propagate along the 0/90 interface. Therefore, we opted to use the term "effective" toughness instead of mode I toughness. We performed an additional study based on finite element simulations, and we found that the maximum mix mode ratio of G_{Ic}/G_c is around 90%. Thus, the measured effective toughness $G_{c,\mathrm{eff}}$ is largely dominated by mode-I fracture toughness, and hence, the test can be a valid method to evaluate mode I behavior.

2.2. Materials and specimens

The materials were aerospace-grade unidirectional carbon fiber/epoxy prepregs (HexPly T700/M21, Hexcel) with a fiber volume

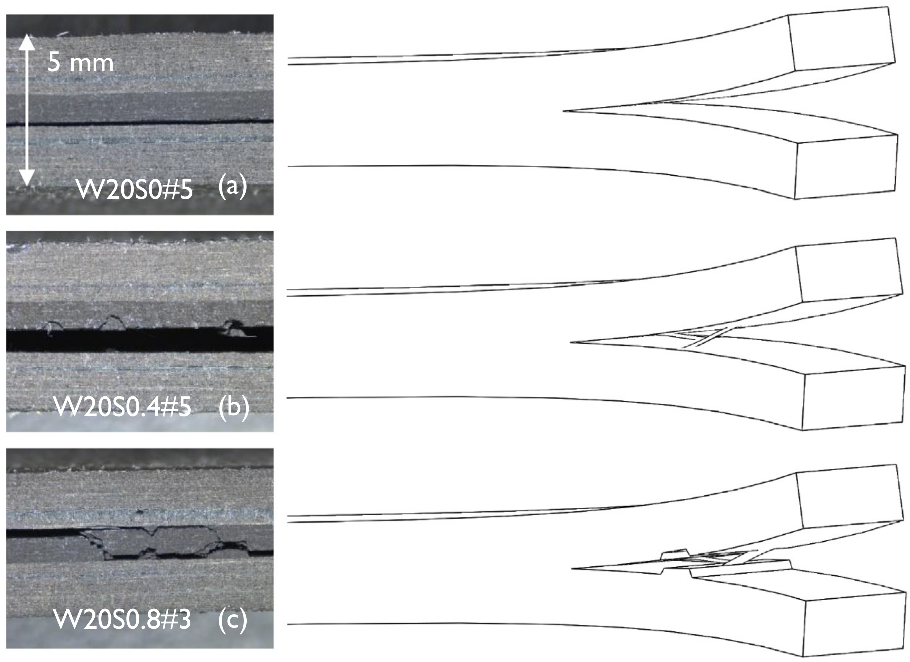

Fig. 5. Side view of the DCB samples using optical microscope. The label W20S0.4#5 means sample with 20 mm width, tensile-tested up to strain of 0.4%, and #5 means the fifth sample of this group. Following this nomenclature, (a), (b), (c), correspond to 0%, 0.4%, and 0.8% in-plane pre-strain respectively.

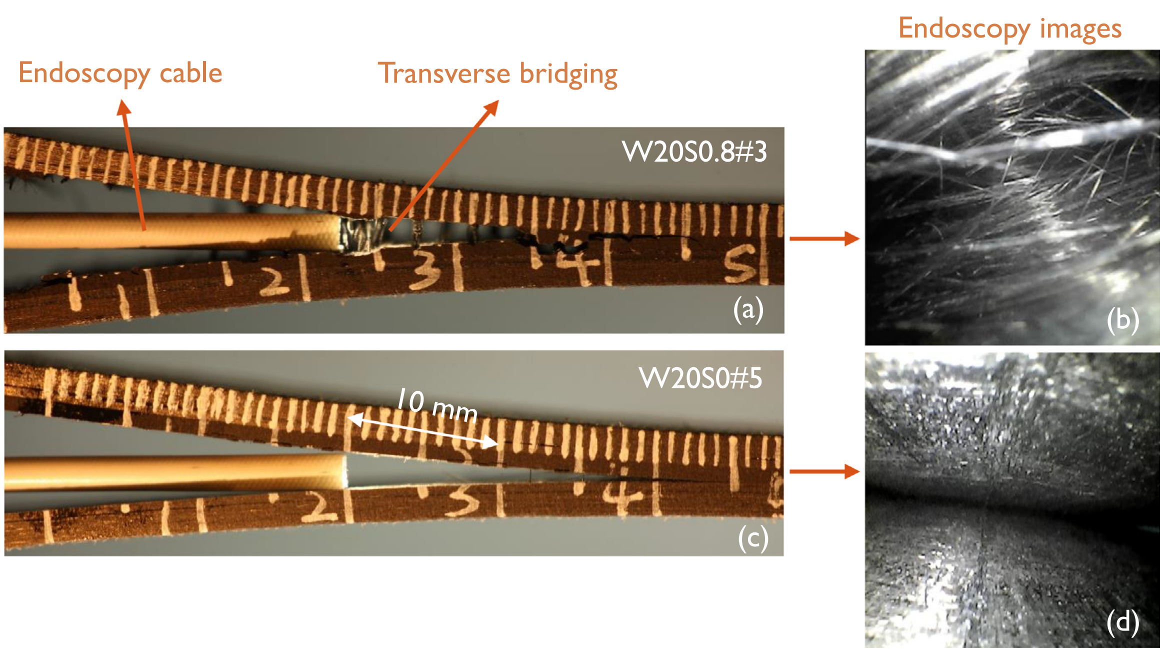

Fig. 6. Endoscopy image at the incremental delamination length around 45 mm for two representative samples. (For interpretation of the references to colour in this figure legend, the reader is referred to the web version of this article.)

fraction of 57% and thickness of 250 microns. First, the $300 \times 300 \text{mm}^2$ prepregs were stacked following the intended stacking sequence. We applied a one bar vacuum to the prepregs to remove trapped air. We then cured the prepregs under a hydraulic hot-press machine (Pinette Emidecau Industries 15T) with a gauge pressure of 7 bar. The pressed prepregs were then heated up from room temperature to 180°C for 2 h with a heating rate of 2°C/min to form a plate. Finally, the plate was cooled down to room temperature at the speed of 3°C/min.

We cut the plate using a Protomax water-jet cutting machine to the intended sample size of 20 mm width and 260 mm length. Note that a single layer of aluminum foil was inserted in the middle of the $[0_2/90_2]_s$ plate to create a 20 mm long pre-crack to accommodate the subsequent DCB test. We chose a 20 mm long pre-crack, instead of the standard 50 mm pre-crack [18], to avoid crushing and slipping due to grip compression while doing the tensile test. For the tensile test, tabs were glued to the sample for proper load transfer. The tabs were cut from a ± 45° glass fiber/epoxy plate. For the DCB test, aluminum blocks were glued to the back-bonded tensile-tested samples ($[0_6||0_2/90_2]_s$). All glue used in this work was Araldite 420 epoxy adhesive. The actual dimension of each sample was recorded for the calculation of interlaminar toughness.

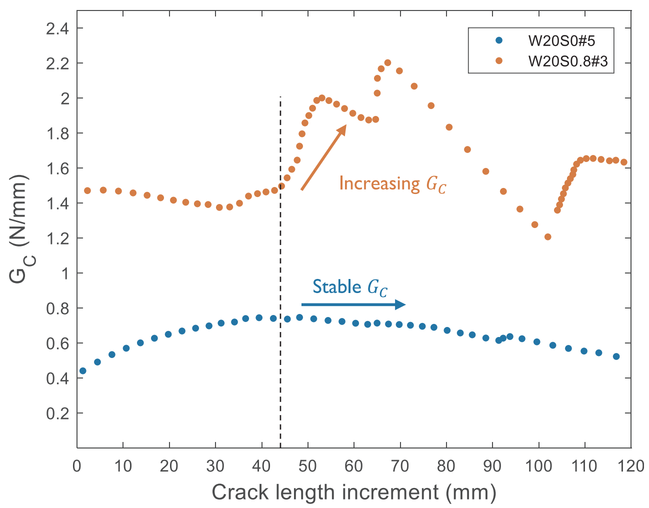

Fig. 7. R-curve of two representative DCB samples with in-plane strain of 0% and 0.8%. (For interpretation of the references to colour in this figure legend, the reader is referred to the web version of this article.)

3. Results and analysis

3.1. Crack density and effective G_c: summary of experimental observations

Fig. 2(a)–(d) show pictures of a sample taken at different locations and different transverse crack densities. The observation zone to calculate transverse crack density is 72 mm wide from the middle of the samples. Since the camera can cover a 4.5 mm wide view, we needed to take 16 pictures for each sample at each strain level.

Fig. 3 illustrates the transverse crack density evolution with respect to in-plane strain levels. Here we defined the transverse crack density ρ as the number of discrete transverse crack N divided by the observation length L and the thickness of the 90° plies H (*i.e.* $\rho = N/(L \times H)$). The data was collected from 10 tensile-tested samples. Five of them were loaded up to 1.4% strain, and the rest were up to 1.2% strain. 1.2% and 1.4% are the strain levels that can cover the whole range of the transverse crack density evolution. Thus, we can already observe a clear trend based on these 10 samples. The first transverse crack initiates around the strain of 0.3%. After the initiation, the transverse crack density increases quickly from the in-plane strain of 0.3% to 0.8%. At strain level higher than 0.8%, the transverse crack density growth rate slows down, revealing a saturation of this mechanism that is a very classical observation [23,28].

We now evaluate the effect of pre-tensile strain level on the interface property (*i.e.* effective fracture toughness). The propagation G_c is based on the average of the measured $G_{c,\text{eff}}$ from an incremental crack length of 50 mm to the end. Fig. 4 shows the evolution of propagation G_c and transverse crack density ρ as the preset in-plane loading increases. The red circles represent the propagation G_c while the blue dots are the transverse crack density. The red and blue solid lines represent parabolic and exponential fitting curves for the evolution of propagation G_c and transverse crack density, respectively. Interestingly, although the transverse crack density monotonically increases, the propagation G_c experiences a parabolic trend with its maximum value around the strain of 0.8%. The propagation G_c increases from 0.2% to 0.8% in-plane strain, which corresponds to the regime where transverse cracking density increases rapidly. Above the strain of 0.8%, the

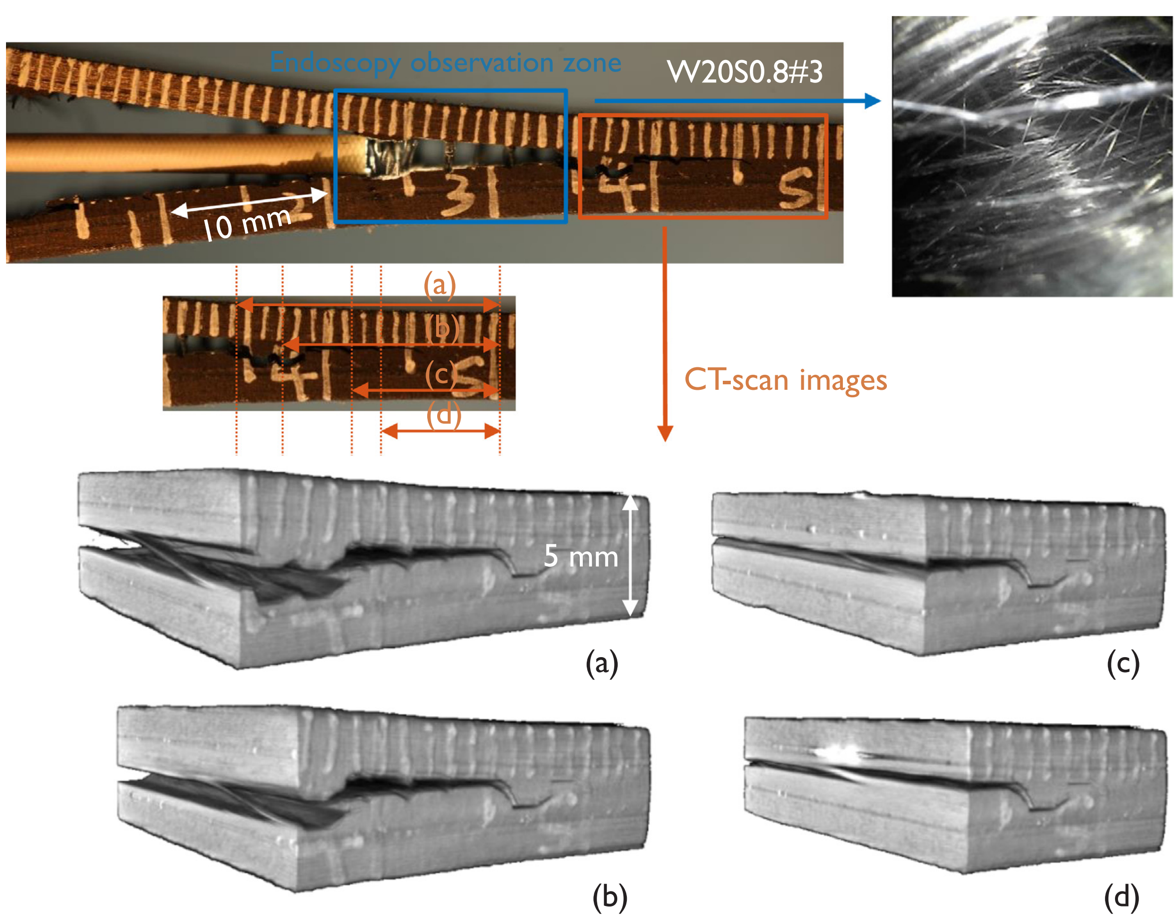

Fig. 8. CT-scan images for representative sample with in-plane strain of 0.8%. (For interpretation of the references to colour in this figure legend, the reader is referred to the web version of this article.)

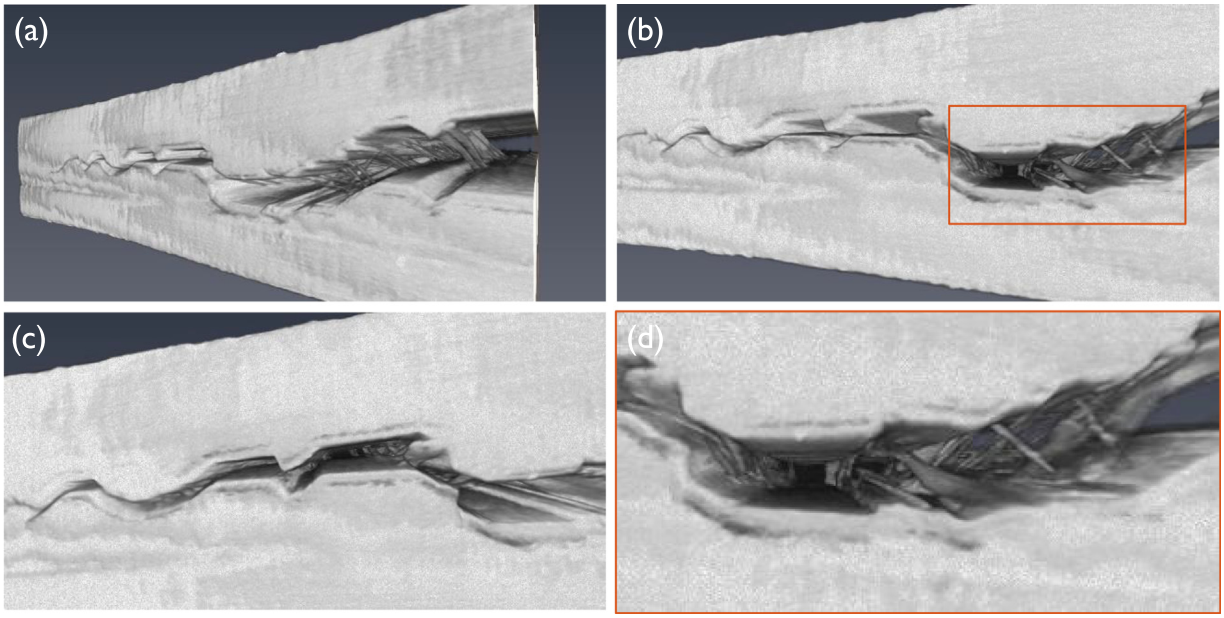

Fig. 9. Different angles to show the transverse bridging of sample W20S0.8#3. (For interpretation of the references to colour in this figure legend, the reader is referred to the web version of this article.)

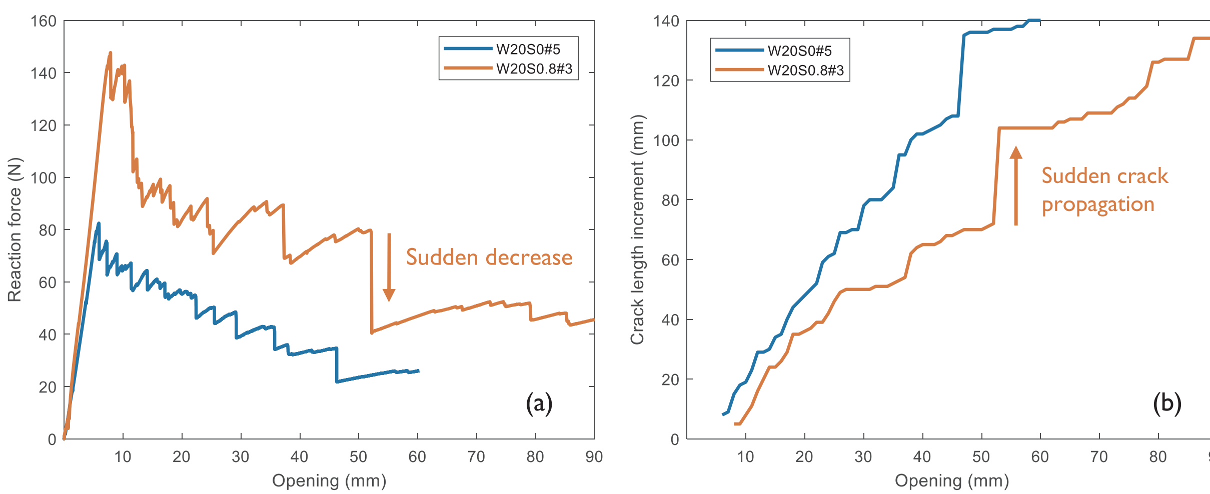

Fig. 10. Original $P-\delta$ curve of two representative samples with in-plane strain of 0% and 0.8%. (For interpretation of the references to colour in this figure legend, the reader is referred to the web version of this article.)

propagation G_c decreases, whereas the transverse crack density stabilizes. Noted that the large increase in G_c, more than 60% between its minimum and maximum values, is expected to play a major role in the propagation of macroscopic delamination. Therefore, understanding this coupling mechanism between in-plane loading and delamination properties is key for designing accurate predictive modeling tools. The parabolic trend in the propagation G_c was unexpected and we present in the following sections a possible explanation based on the competition between the transverse-cracking-induced fiber bridging and transverse-cracking-induced local delamination.

3.2. Analysis of the side-view morphology

We investigated the fracture morphology of DCB samples from the side view using an optical microscope to understand the cause of this parabolic evolution of G_c as described above. Fig. 5(a)–(c) show the side view of a representative sample selected from various in-plane strain levels (*i.e.*, 0%, 0.4%, and 0.8%). It shows that various fracture modes may occur for different in-plane strain levels. For example, in samples with a low in-plane strain level (*i.e.* below 0.2%), the delamination crack propagates along with the 0/90 interface, leaving a smooth fracture surface. There was no migration observed during the delamination process. We observed limited transverse and 0° bridging. Here we defined a transverse bridging as fibers connecting upper and lower surface in a 90° (transverse to loading) direction.

For samples with an in-plane strain of 0.4%, there were several migrations observed during the delamination propagation due to the initiation of transverse cracks introduced during the tensile tests. Such bridging is probably due to the transverse cracks, introduced in 90° plies, which promote random strength (defect) distributions. This opens possibilities to form bridging, which results in an increase of G_c.

At higher in-plane strain levels (from 0.4% to 1.0%), the density of transverse cracks increases dramatically, and thus, the spacing between the two adjacent transverse cracks becomes smaller. More migration attempts and random damage are introduced, which finally resulted in more opportunities to form transverse bridging. Thus the propagation G_c increases with the growth of transverse crack density. With a further increase of the in-plane strain (above 1.0%), the transverse crack density

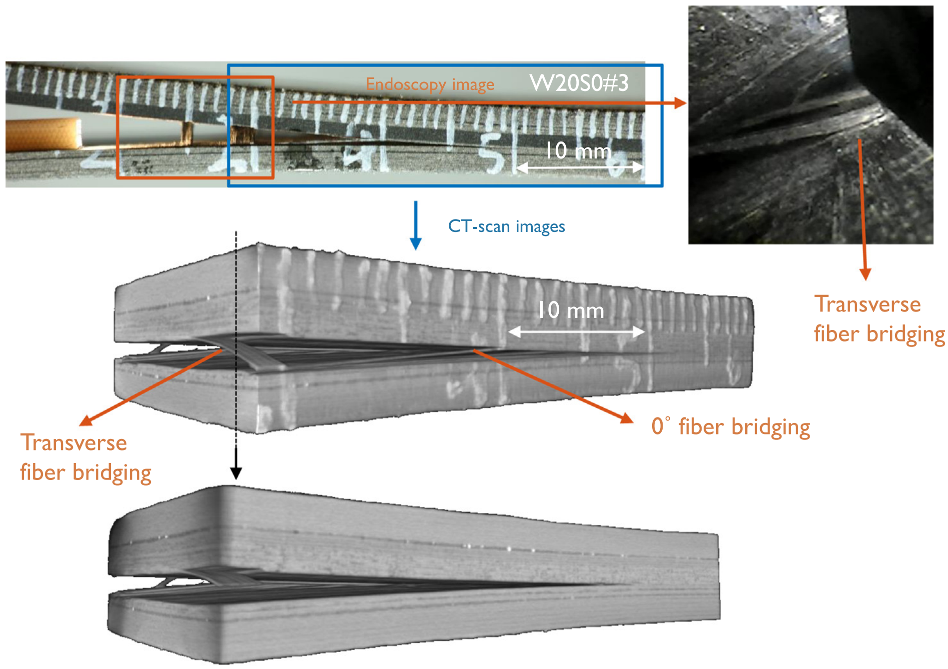

Fig. 11. Endoscopy and CT-scan images for sample W20S0#3. (For interpretation of the references to colour in this figure legend, the reader is referred to the web version of this article.)

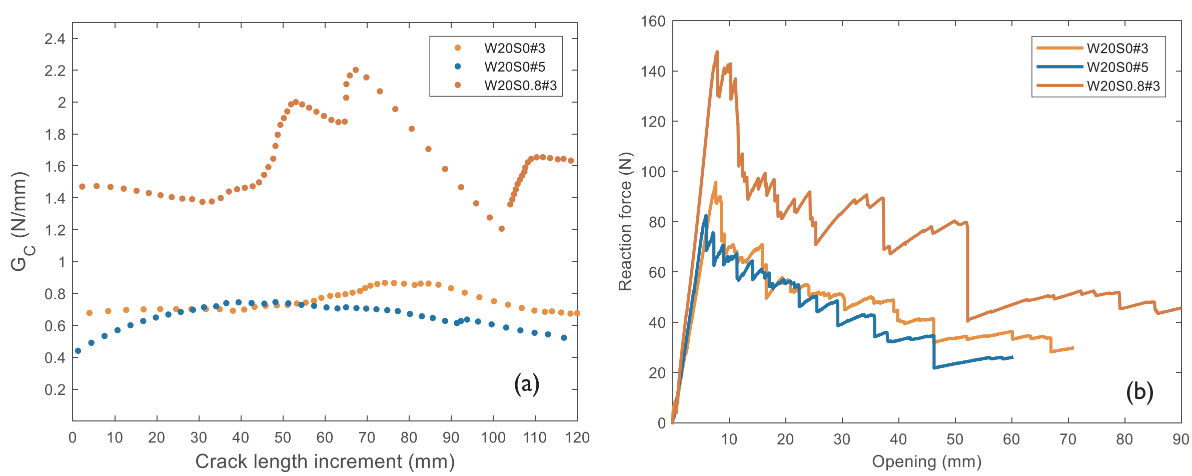

Fig. 12. R-curve and $P-\delta$ curve for representative samples with in-plane strain of 0% and 0.8%. (For interpretation of the references to colour in this figure legend, the reader is referred to the web version of this article.)

gradually reaches a saturation limit. In this case, the spacing does not increase anymore, yet the local delamination may appear. Such local delamination reduces the effective bonding area between the 0/90 interface. This finally leads to a decrease of propagation G_c.

3.3. Fiber bridging analysis

Our previous results suggest that transverse bridging strengthens the effective toughness. However, it is difficult to justify the presence of fiber bridging just by using side-view images. In this subsection, we performed *in-situ* endoscopy imaging and a computed tomography CT-scan to observe the fracture morphology around the delamination tip. The endoscopy is non-intrusive as we were very careful to not perturbate the loading or the degradation pattern during observations of the crack tip.

3.3.1. Endoscopy image

Fig. 6 shows two representative DCB samples (W20S0.8#3 and W20S0#5) with preset in-plane strains of 0.8% and 0%, respectively. This shows a clear difference in damage phenomenology between the two samples. With low levels of in-plane strain, the delamination crack tip is quite clean and smoothly goes between the 0/90 interface (Fig. 6(c)–(d)). For the in-plane strain of 0.8%, there are quite a lot of migration attempts. Extensive transverse bridging is introduced during the DCB test. The massive transverse bridging that connects the top and bottom beam in Fig. 6(b) primarily strengthens the local toughness and participates in the development of a larger process zone, thus ensuring more dissipation when bridging is activated as a non-local dissipating mechanism [29]. Fig. 7 shows the R-curve of these two representative samples. With extensive transverse bridging (when the crack tip reaches 45 mm) in sample W20S0.8#3, the G_c increases significantly from 45 mm to 55 mm. While for the sample of W20S0#5, in which no transverse bridging is formed, the R-curve is more flat and stable,

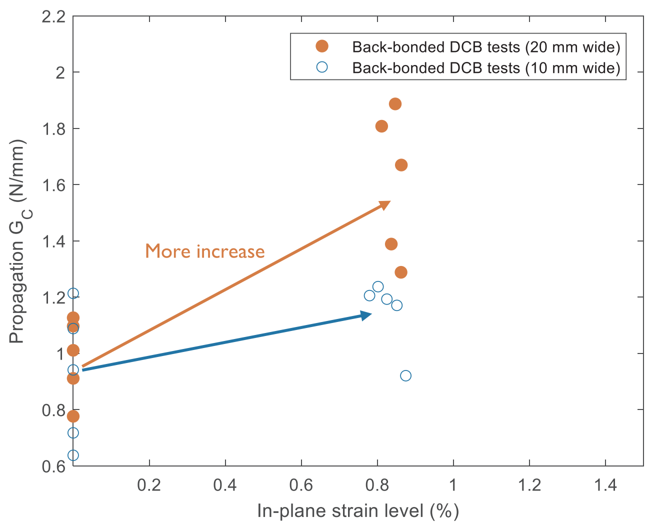

Fig. 13. Propagation G_c comparison with in-plane strain of 0% and 0.8% for two different widths. (For interpretation of the references to colour in this figure legend, the reader is referred to the web version of this article.)

revealing a constant dissipation only ascribed to the local separation of the interface.

3.3.2. CT-scan image

In the previous subsection, endoscopy imaging reveals the existence of transverse bridging, as in Fig. 6(b) for sample W20S0.8#3. We used a computed tomography (CT) in sample W20S0.8#3 to take a closer observation of the delamination crack tip. We stopped the DCB test when the crack tip reached 49 mm and maintained the opening by inserting a block in the mouth of the sample. Then we removed the sample from the loading frame and put it into the CT room. Fig. 8(a)–(d) show the cross-section of different positions from 35 mm to 49 mm, where crude fiber cluster can be seen connecting the top and bottom beam. Fig. 9(a)–(c) show the transverse bridging from different angles, which clearly prove the extensive transverse bridging of fiber clusters.

Fig. 7 shows that the R-curve of sample W20S0.8#3 fluctuates significantly, unlike the normal case where the dissipation increases with the crack propagation and gradually reaches a stable value. This fluctuation is due to the formation and breakage of the transverse bridging zone. Fig. 10(a) shows the original P - δ curve of sample W20S0.8#3 and W20S0#5. From the opening of 40 mm to 52 mm for sample W20S0.8#3, the reaction force increases monotonically, whereas the crack length does not increase. During this period, the energy is stored through fiber bridging formation and as elastic energy in the created bundles. Once the stored energy reaches its critical threshold (that we see here when the opening reaches 52 mm), the bridging breaks abruptly and the crack propagates instantaneously. This results in a sudden decrease in the reaction force. Such a process is then repeated several times until the whole DCB sample delaminates.

For the samples with 0% in-plane strain, the delamination crack propagates smoothly between the 0/90 interface. In this case, we observed minimal transverse bridging and 0° bridging from CT-scan images. Fig. 11 shows the limited transverse bridging and 0° bridging in sample W20S0#3. The toughness and reaction force of sample W20S0#3 is still at the same level as sample W20S0#5, (Fig. 12)). This confirmed our finding by using the side-view images obtained by an optical microscope.

3.4. Width effect on the transverse bridging

As we proved that the increase of propagation G_c of samples with in-plane strain up to 0.8% is due to the creation of transverse bridging, we expected the extra dissipation provided by such transverse bridging to be width-dependent. We performed additional tests with a sample width of 10 mm. Two strain levels (0% and 0.8%) were tested to confirm the hypothesis. Fig. 13 compares the propagation G_c of 10 mm and 20 mm samples. For the 10 mm wide samples, the increase of G_c from 0% to 0.8% is much smaller compared to the 20 mm wide samples. Wider samples provide longer transverse bridging, which requires more energy to break. Thus, the larger the width of the samples, the higher propagation G_c observed. This result also proves our theory that the increase of propagation G_c from 0% to 0.8% in-plane strain is mainly due to the transverse bridging zone. The effect of the transverse bridging zone can be removed using a very narrow width sample.

4. Conclusions

We studied the influence of intralaminar damage on effective interlaminar properties through a novel two-step mechanical test. First, we performed a tensile test on the $[0_2/90_2]_s$ cross-ply laminates to introduce various extents of intralaminar damage. Next, we bonded a backing adherend of $[0_6]$ plies to the cross-ply, followed by a double cantilever beam test. With different levels of intralaminar damage introduced into the middle 90° plies, the delamination propagated in various modes.

For a lower level of in-plane strain when there was no transverse crack initiated inside the 90° plies, the delamination propagates along with the 0/90 interface leaving a smooth fracture surface. We observed only limited 0° fiber bridging and transverse bridging.

For intermediate in-plane strain levels (from 0.4% to 1.0%), the transverse crack density increased rapidly. More migration and random strength/defect distributions were produced. This facilitated the formation of extensive transverse bridging, leading to a strengthening of the toughness significantly by the introduction of a new non-local dissipation mechanism.

At further in-plane strain levels (from 1.0% to 1.4%), the transverse crack density was saturated and hence, the spacing between transverse crack did not change anymore. At this stage, the local delamination started to occur, leading to a decrease in the effective bonding area. Thus, the propagation G_c started to decrease.

Interestingly, introducing damage will, in turn, unexpectedly increase the interfacial toughness of the laminates. The remarkable variation in the macroscopic delamination properties makes the modeling of such effects relevant when a predictive model is targeted. Our results highlight some limitations of classical mesoscale damage mechanics that assumes the toughness to be a material property. In fact, toughness should be considered function of both the local lay-up and of the damage of the plies surrounding the interface. Different strategies can be adopted to model such effects from a macroscopic point of view, like developing specific cohesive elements that would explicitly introduce the effect of cracking density of adjacent plies on the interlaminar toughness. The data provided in this paper represent the first step towards the design of improved models that will be discussed in future publications.

CRediT authorship contribution statement

Ping Hu: Formal analysis, Writing - original draft. **Ditho Pulungan:** Data curation, Writing - review & editing. **Ran Tao:** Visualization, Writing - review & editing. **Gilles Lubineau:** Conceptualization, Supervision, Writing - review & editing.

Declaration of Competing Interest

The authors declare that they have no known competing financial interests or personal relationships that could have appeared to influence the work reported in this paper.

Acknowledgement

The research reported in this publication was supported by funding from King Abdullah University of Science and Technology (KAUST) Baseline Research Funds, under award number BAS/1/1315-01-01.

References

[1] Ladeveze P, LeDantec E. Damage modelling of the elementary ply for laminated composites. Compos Sci Technol 1992;43(3):257–67.
[2] Lubineau G, Ladeveze P. Construction of a micromechanics-based intralaminar mesomodel, and illustrations in abaqus/standard. Comput Mater Sci 2008;43(1):137–45.
[3] Hallett SR, Green BG, Jiang WG, Wisnom MR. An experimental and numerical investigation into the damage mechanisms in notched composites. Compos. Part A: Appl. Sci. Manuf. 2009;40(5):613–24.
[4] Abrate S. Impact on composite structures. Cambridge University Press; 2005.
[5] Wagih A, Maimí P, Blanco N, Costa J. A quasi-static indentation test to elucidate the sequence of damage events in low velocity impacts on composite laminates. Compos Part A: Appl Sci Manuf 2016;82:180–9.
[6] Topac OT, Gozluklu B, Gurses E, Coker D. Experimental and computational study of the damage process in cfrp composite beams under low-velocity impact. Compos Part A: Appl Sci Manuf 2017;92:167–82.
[7] Thorsson SI, Waas AM, Rassaian M. Low-velocity impact predictions of composite laminates using a continuum shell based modeling approach part a: Impact study. Int J Solids Struct 2018;155:185–200.
[8] Talreja R, Phan N. Assessment of damage tolerance approaches for composite aircraft with focus on barely visible impact damage. Compos Struct 2019;219:1–7.
[9] Zubillaga L, Turon A, Renart J, Costa J, Linde P. An experimental study on matrix crack induced delamination in composite laminates. Compos Struct 2015;127:10–7.
[10] Kashtalyan M, Soutis C. Analysis of composite laminates with intra- and interlaminar damage. Prog Aerosp Sci 2005;41(2):152–73.
[11] Abisset E, Daghia F, Sun XC, Wisnom MR, Hallett SR. Interaction of inter-and intralaminar damage in scaled quasi-static indentation tests: Part 1–experiments. Compos Struct 2016;136:712–26.
[12] Johnson P, Chang FK. Characterization of matrix crack-induced laminate failure—part i: Experiments. J Compos Mater 2001;35(22):2009–35.
[13] Canal LP, Alfano M, Botsis J. A multi-scale based cohesive zone model for the analysis of thickness scaling effect in fiber bridging. Compos Sci Technol 2017;139:90–8.
[14] Sebaey TA, Blanco N, Costa J, Lopes CS. Characterization of crack propagation in mode i delamination of multidirectional cfrp laminates. Compos Sci Technol 2012;72(11):1251–6.
[15] De Moura MFSF, Campilho RDSG, Amaro AM, Reis PNB. Interlaminar and intralaminar fracture characterization of composites under mode i loading. Compos Struct 2010;92(1):144–9.
[16] Farmand-Ashtiani E, Cugnoni J, Botsis J. Specimen thickness dependence of large scale fiber bridging in mode i interlaminar fracture of carbon epoxy composite. Int J Solids Struct 2015;55:58–65.
[17] Huchette C, Vandellos T, Laurin F. Influence of intralaminar damage on the delamination crack evolution. Damage growth in aerospace composites. Springer; 2015. p. 107–40.
[18] ASTMD5528. Standard test method for mode I interlaminar fracture toughness of unidirectional fiber-reinforced polymer matrix composites. ASTM Internat; 2007.
[19] Manders PW, Chou TW, Jones FR, Rock JW. Statistical analysis of multiple fracture in 0/90/0 glass fibre/epoxy resin laminates. J Mater Sci 1983;18(10):2876–89.
[20] Crossman FW, Wang ASD. The dependence of transverse cracking and delamination on ply thickness in graphite/epoxy laminates. In: Damage in composite materials: basic mechanisms, accumulation, tolerance, and characterization. ASTM International; 1982.
[21] Lafarie-Frenot MC, Henaff-Gardin CBAE. Influence of zinc iodide penetrant on damage evolution in cfrp laminates. Adv Compos Lett 1993;2(1):21–4.
[22] Cowley KD, Beaumont PWR. Damage accumulation at notches and the fracture stress of carbon-fibre/polymer composites: combined effects of stress and temperature. Compos Sci Technol 1997;57(9–10):1211–9.
[23] Groves SE, Harris CE, Highsmith AL, Allen DH, Norvell RG. An experimental and analytical treatment of matrix cracking in cross-ply laminates. Exp Mech 1987;27(1):73–9.
[24] Nairn JA. Matrix microcracking in composites. Polym Matrix Compos 2000;2:403–32.
[25] Palmieri FL, Hopkins J, Wohl CJ, Lin Y, Connell JW, Belcher MA, et al. Laser surface preparation of epoxy composites for secondary bonding: Optimization of ablation depth; 2015.
[26] Mahendrarajah G, Kandare E, Khatibi AA. Enhancing the fracture toughness properties by introducing anchored nano-architectures at the metal–frp composite interface. J Compos Sci 2019;3(1):17.
[27] Saenz EE, Carlsson LA, Salivar GC, Karlsson AM. Fatigue crack propagation in polyvinylchloride and polyethersulfone polymer foams. J Sandwich Struct Mater 2014;16(1):42–65.
[28] Berthelot JM. Transverse cracking and delamination in cross-ply glass-fiber and carbon-fiber reinforced plastic laminates: static and fatigue loading. Appl Mech Rev 2003;56(1):111–47.
[29] Canal LP, Pappas G, Botsis J. Large scale fiber bridging in mode i intralaminar fracture. an embedded cell approach. Compos Sci Technol 2016;126:52–9.